

# A higher order approximate static condensation method for multi-material diffusion problems

Alexander Zhiliakov\*    Daniil Svyatskiy<sup>†</sup>    Maxim Olshanskii<sup>‡</sup>  
Evgeny Kikinon<sup>§</sup>    Mikhail Shashkov<sup>¶</sup>

August 8, 2019

## Abstract

The paper studies an approximate static condensation method for the diffusion problem with discontinuous diffusion coefficients. The method allows for a general polygonal mesh which is unfitted to the material interfaces. Moreover, the interfaces can be discontinuous across the mesh edges as typical for numerical reconstructions using the volume or moment-of-fluid methods. We apply a mimetic finite difference method to solve local diffusion problems and use  $P_1$  (mortar) edge elements to couple local problems into the global system. The condensation process and the properties of the resulting algebraic system are discussed. It is demonstrated that the method is second order accurate on smooth solutions and performs well for problems with high contrast in diffusion coefficients. Experiments also show the robustness with respect to position of the material interfaces against the underlying mesh.

## 1 Introduction

Multi-phase and multi-material processes are ubiquitous in nature and engineering. Mathematical models of such processes are often formulated in terms of systems of partial differential equations with discontinuous coefficients and interface conditions on time-dependent internal boundaries. Due to their high complexity, these models defy analytical treatment, and hence numerical simulations became an indispensable tool for solving the models and gaining insights into underlying phenomena.

Past decades evidenced an explosive [growth in the development of efficient computational techniques](#) for problems with evolving interfaces, which involve interaction between many materials or different phases of matter. These developments include immersed boundary method [?], immersed interface method [?], and unfitted finite element methods [?, ?], to name several popular numerical approaches. Depending on how the interface is treated

---

\*Department of Mathematics, University of Houston, Houston, Texas 77204 (alex@math.uh.edu).

<sup>†</sup>Los Alamos National Laboratory, Los Alamos, New Mexico, USA (dasvyat@lanl.gov).

<sup>‡</sup>Department of Mathematics, University of Houston, Houston, Texas 77204 and Sechenov University, Moscow (molshan@math.uh.edu); Partially supported by NSF through grant DMS-1717516.

<sup>§</sup>Los Alamos National Laboratory, Los Alamos, New Mexico, USA (kikinon@lanl.gov).

<sup>¶</sup>Los Alamos National Laboratory, Los Alamos, New Mexico, USA (shashkov@lanl.gov).

numerically, one can distinguish between methods that smear the interface over a strip of finite thickness which should be further resolved by the mesh, like in the phase field approach [?], and methods that use a sharp interface representation, as in the level-set method [?]. If one applies a sharp representation to handle complex geometries or interfaces undergoing large deformations, it is convenient to allow the interface to cut through the background mesh in an arbitrary way. In turn, this leads to the problem of building accurate and stable approximations for so-called multi-material cells, i.e. the mesh cells intersected by material interfaces. In particular, one is interested in discretizations which are robust with respect to how interfaces intersect the mesh and with respect to the contrast of material properties, e.g. the ratio of physical parameters. This is the setting and the problem we focus in this paper.

One standard approach to handle multi-material cells is a homogenization procedure. In this approach, one assigns to the cells artificial homogeneous material properties, which are calculated based on the volumetric shares of different materials in each of the multi-material cells. This enables one to apply standard discretization techniques. Further one recovers solution in each phase from the computed cell-averaged values [?]. Although being technologically straightforward, the homogenization approach often fails to accurately model subcell material interactions, which results in non-physical numerical solutions to problems with high-contrast material properties.

As an alternative to the homogenization, one may reconstruct interfaces in each multi-material cell using a piecewise planar approximation. In this case, single-material domains in the cell are non-overlapping polytopes that typically preserve known material volumes. In this paper, we deal with interfaces reconstructed by the volume-of-fluid (VOF) [?] method, which is a commonly used numerical approach to recover interface location. The approach includes the moment-of-fluid (MOF) methods [?] that generally provide better accuracy if centroids of material subdomains are known. For the numerical experiments here we apply the extended MOF [?] to construct local meshes inside multi-material cells such that subcell contains only one material and all information about the local topology is available.

The conservation properties of the VOF and MOF approaches, however, come at a price of recovering a piecewise planar interface approximation that is discontinuous across the faces of the background computational mesh. One technique to deal with this issue consists in including the local tessellations into the global computational mesh, thus effectively refining the mesh so that every cell contains only one material [?]. This turns out to be a non-trivial computational geometry problem, and the resulting mesh in 2D often contains very small and co-linear faces, while the extension of this approach to 3D does not seem feasible for general unstructured meshes.

In this paper, we devise a higher order method for the numerical solution of the diffusion problem with discontinuous coefficients on polytopal meshes with multi-material cells. We assume that interface reconstruction is performed using the extended MOF method, which provides local single-material meshes with full topological data. One might consider solving this problem with Nitsche's methods used in the framework of cut-cells [?, ?] or extended finite element methods (X-FEM) [?]. However, these methods are typically not locally conservative and the discontinuity of material interfaces across faces of multi-material cells can be large enough to result in a significant loss of accuracy.

The present method builds upon the approximate static condensation (ASC) algorithm proposed in [?]; it admits high-contrast diffusion coefficients and discontinuous reconstruction of the interfaces. The ASC approach uses the formulation of the interface diffusion problem as a system of problems on local meshes that are coupled through the concentration values and fluxes on the faces of multi-material cells. This face concentration serves as a new primal unknown and it is further approximated by piecewise polynomial functions defined on all faces of the global (unfitted polygonal) mesh. The original paper [?] considered  $P_0$  (piecewise constant) approximation to the face concentration, while the present study introduces higher order polynomials for this purpose. Although the latter potentially leads to more accurate results (and in some cases we shall see that it provides convergent results, when the  $P_0$  version fails), it also raises some questions about stability and robustness, which we address in the present report. We note that using a skeleton space of piecewise polynomial functions to couple local unknowns renders the approach as a version of a mortar method [?, ?], although mortar finite element methods were developed for different types of problems and substantially vary in terms of implementation.

The approximate static condensation approach leaves much freedom in the choice of the discretization method for the local diffusion problems. Posed in each polygonal cell, these problems are given by diffusion equations with discontinuous coefficients. The method benefits from the observation that for any fixed cell  $T$ , material interfaces, which possibly intersect with  $T$ , induce a *consistent polygonal subdivision* (local mesh) of  $T$ . Opposite to the global mesh, the local one is *fitted* to interfaces, i.e. each micro polyhedral element is shared only by one material. Following [?], we apply the mimetic finite difference (MFD) method from [?] to approximate the local diffusion problems on this fine fitted mesh. After eliminating inter-cell degrees of freedom (d.o.f.), one obtains a system of linear algebraic equations for the face concentration degrees of freedom. The fluxes and inter-element degrees of freedom are recovered by simple postprocessing. Further, we study the performance of the method in terms of accuracy, robustness with respect to the interfaces position, and algebraic stability.

The remainder of the paper is organized as follows. In section 2 we formulate the model diffusion problem with discontinuous diffusion tensor, introduce the basic mesh and discuss a reformulation of the model as a system of coupled local problems. Section 3 presents the method and discusses certain properties of the resulting system of algebraic equations. Finally, section 4 collects results of numerical experiments. These results include accuracy tests, numerical comparison with the method from [?] and with a homogenization method as the alternative approach.

## 2 Model problem and macro-mesh decomposition

In a polygonal bounded domain  $\Omega \subset \mathbb{R}^2$  we consider the following diffusion problem in the mixed form

$$\begin{cases} \mathbf{K}^{-1} \mathbf{u} + \nabla p = 0 & \text{in } \Omega, \\ \nabla \cdot \mathbf{u} + c p = f & \text{in } \Omega \end{cases} \quad (1)$$

with boundary data

$$p = g_D \quad \text{on } \partial\Omega_D, \quad \mathbf{u} \cdot \hat{\mathbf{n}} = g_N \quad \text{on } \partial\Omega_N. \quad (2)$$

Here  $p$  is a concentration and  $\mathbf{u}$  is the diffusive flux,  $\mathbf{K}$  is the positive definite symmetric diffusivity tensor, which we assume constant within each material subdomain,  $c \geq 0$  is the reaction coefficient,  $\hat{\mathbf{n}}$  is the outward normal vector to  $\partial\Omega$ ,  $g_D$  and  $g_N$  are Dirichlet and Neumann boundary data, respectively. In the context of fluid flows in porous media, (1)–(2) is also known as the Darcy problem. In this case,  $p$  has the meaning of pressure,  $\mathbf{u}$  is fluid velocity, and  $\mathbf{K}$  is the permeability tensor.

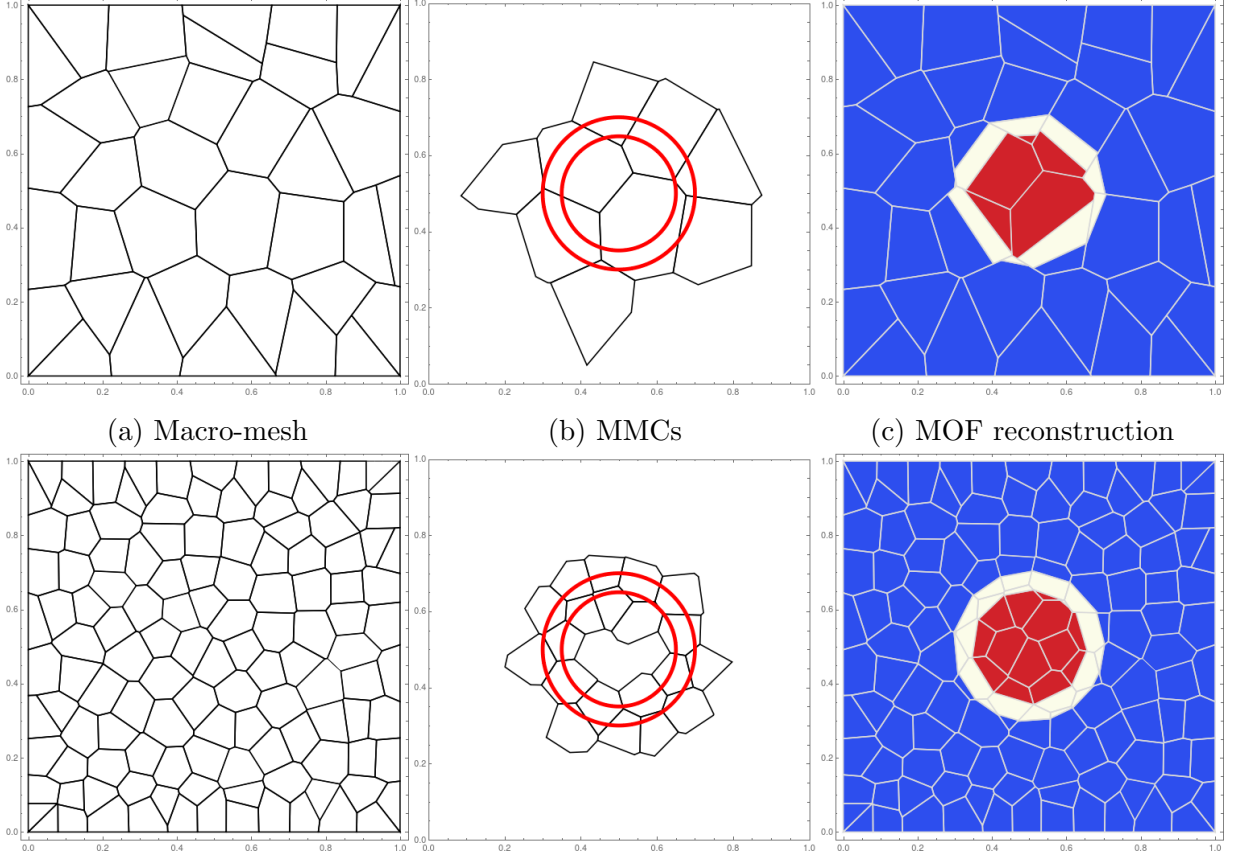


Figure 1: The figure illustrates global unstructured polyhedral mesh (left); Physical interfaces for three materials and cut cells, i.e. multi-material cells (central); The piecewise-planar discontinuous reconstruction of the interfaces by the moment-of-fluid method (right). Everything is shown for two refinement levels of the macro-mesh

We assume the triangulation  $\mathcal{T}$  of  $\Omega$  consisting of general polyhedral elements as illustrated in Figure 1 (left). This triangulation constitutes our macro-mesh. The material interfaces, i.e. surfaces where  $\mathbf{K}$  may experience discontinuities, may cut through the macro-mesh in an arbitrary way; see Figure 1 (center). The polygonal cells  $T \in \mathcal{T}$  cut by the interfaces are further called multi-material cells (MMCs). In practice, we are given a reconstructed interface by a volume-of-fluid or moment-of-fluid method. This reconstructed interface may be discontinuous across faces of MMCs, but locally within each  $T \in \mathcal{T}$  it is a collection of planar surfaces; see Figure 1 (right).

Denote by  $\mathcal{F}$  the collection of all faces of the macro-mesh  $\mathcal{T}$ . We shall distinguish between the subset of internal and external faces,  $\mathcal{F} = \mathcal{F}_{\text{int}} \cup \mathcal{F}_{\text{ext}}$ <sup>1</sup>. Introducing the new unknown

<sup>1</sup>For the sake of notation, we shall use  $\mathcal{F}$  to denote both the set of elements and the corresponding

$\lambda \in \mathbb{H}^{\frac{1}{2}}(\mathcal{F})$ , we reformulate (1)–(2) as a system of local problems coupled through the boundary data and flux continuity condition:

$$\begin{cases} \mathbf{K}^{-1} \mathbf{u} + \nabla p = 0 & \text{in } T, \\ \nabla \cdot \mathbf{u} + c p = f & \text{in } T, \\ p = \lambda & \text{on } \partial T, \end{cases} \quad \forall T \in \mathcal{T}, \quad (3)$$

$$[[\mathbf{u} \cdot \hat{\mathbf{n}}]] = 0 \quad \text{on } F, \quad \forall F \in \mathcal{F}_{\text{int}}. \quad (4)$$

Here  $\hat{\mathbf{n}}$  denotes a normal vector to the face  $F \in \mathcal{F}_{\text{int}}$  and  $[[\mathbf{u} \cdot \hat{\mathbf{n}}]]$  is the jump of the normal flux across  $F$ . On the outer boundary  $\partial\Omega$  we assume (2).

Note that  $\lambda$  defines Dirichlet boundary data for local diffusion problems. Once  $\lambda$  is known, one can solve (3) for  $\mathbf{u}$  and  $p$  inside each element independently, and hence recover the solution of the original problem (1). The idea behind the ASC method is to introduce a piecewise polynomial space to approximate  $\lambda$ , and define discretizations of subproblems from (3). These local subproblems are further explicitly resolved to eliminate internal degrees of freedom and to form a system of algebraic equations for  $\lambda$ .

Before we go into details of the method, we note that  $\lambda$  can also be observed as the Lagrange multiplier corresponding to the normal flux condition (4). The problem (3)–(4) can be formulated in the weak form: Find  $\mathbf{u} \in \bigotimes_{T \in \mathcal{T}} \mathbb{H}_{\text{div}}(T)$  s.t.  $\mathbf{u} \cdot \hat{\mathbf{n}} = g_N$  on  $\partial\Omega_N$ ,

$p \in \mathbb{L}^2(\Omega)$ ,  $\lambda \in \mathbb{H}^{\frac{1}{2}}(\mathcal{F}_{\text{int}})$  such that

$$\begin{aligned} \int_{\Omega} \mathbf{K}^{-1} \mathbf{u} \cdot \mathbf{v} \, d\mathbf{x} - \sum_{T \in \mathcal{T}} \int_T p \nabla \cdot \mathbf{v} \, d\mathbf{x} + \sum_{F \in \mathcal{F}_{\text{int}}} \int_F \lambda [[\mathbf{v} \cdot \hat{\mathbf{n}}]] \, dl &= - \int_{\partial\Omega_D} g_D \mathbf{v} \cdot \hat{\mathbf{n}} \, dl, \\ \sum_{T \in \mathcal{T}} \int_T \nabla \cdot \mathbf{u} \, q \, d\mathbf{x} + \int_{\Omega} c p \, q \, d\mathbf{x} &= \int_{\Omega} f \, q \, d\mathbf{x}, \\ \sum_{F \in \mathcal{F}_{\text{int}}} \int_F [[\mathbf{u} \cdot \hat{\mathbf{n}}]] \, \mu \, dl &= 0 \end{aligned} \quad (5)$$

for all  $\mathbf{v} \in \bigotimes_{T \in \mathcal{T}} \mathbb{H}_{\text{div}}(T)$  s.t.  $\mathbf{v} \cdot \hat{\mathbf{n}} = 0$  on  $\partial\Omega_N$ ,  $q \in \mathbb{L}^2(\Omega)$ , and  $\mu \in \mathbb{H}^{\frac{1}{2}}(\mathcal{F}_{\text{int}})$ .

### 3 Approximate static condensation method

In this section we describe approximate static condensation method of order  $n$ , ASC( $n$ ), for solving the multi-material heterogeneous diffusion problem (1).

Consider an arbitrary but fixed cell  $T \in \mathcal{T}$ . We now introduce the discretization of the local diffusion problem (3) in  $T$ . To this end, we consider the local mesh  $\boldsymbol{\tau}(T)$  of  $T$ , which is referred as mini-mesh. While the original triangulation  $\mathcal{T}$  is referred as macro-mesh. If  $T$  contains only one phase or material, then we obviously have  $\boldsymbol{\tau}(T) = \{T\}$ . Otherwise for the cell

---

domain formed by their union  $\cup_{F \in \mathcal{F}} \bar{F}$ ; same for  $\mathcal{F}_{\text{int}}$ ,  $\mathcal{F}_{\text{ext}}$  and other collections of mesh elements introduced later in the text. The meaning should be clear from a context.



shared by several phases,  $\tau(T)$  consists of polygonal elements, forming a tessellation of  $T$ , such that any  $\tau \in \tau(T)$  contains only one phase/material; see Figure 2. We denote by  $\mathbf{f}(T)$  the set of all faces in  $\tau(T)$ , which collects both internal and boundary (external) faces with respect to  $T$ ,  $\mathbf{f}(T) = \mathbf{f}_{\text{int}}(T) \cup \mathbf{f}_{\text{ext}}(T)$ . If the meaning is not obvious from the context, we will refer to elements of  $\mathbf{f}(T)$  as “mini-faces,” and to elements of  $\mathcal{F}$  as “macro-faces.” Thus for the example of local mesh drafted in Figure 2, we have three elements in  $\tau(T)$ , two internal faces from  $\mathbf{f}_{\text{int}}(T)$  and eleven external faces from  $\mathbf{f}_{\text{ext}}(T)$ . It is clear that this local mesh is fitted to the material interfaces.

We shall discretize (3) in  $T$  in terms of average fluxes assigned to each face from  $\mathbf{f}(T)$ , we denote the corresponding vector by  $\mathbf{u}_\tau \in \mathbb{R}^{n_f}$ ,  $n_f = \#\mathbf{f}(T)$ , and concentration values assigned to each cell  $\tau \in \tau(T)$ , we denote the corresponding vector by  $\mathbf{p}_\tau \in \mathbb{R}^{n_p}$ ,  $n_p = \#\tau(T)$ . The given data is the source term vector  $\mathbf{f}_\tau \in \mathbb{R}^{n_p}$  and the concentration values  $\lambda$  on the boundary of  $T$ . To approximate this boundary data *for the local problem*, we introduce the vector  $\boldsymbol{\lambda}_\tau \in \mathbb{R}^{n_\lambda}$ ,  $n_\lambda = \#\mathbf{f}_{\text{ext}}(T)$ , where we assign one averaged concentration value for each  $f \in \mathbf{f}_{\text{ext}}(T)$ , so that  $\boldsymbol{\lambda}_\tau$  can be seen as a piecewise-constant approximation of  $\lambda$  with respect to the subdivision of  $\partial T$  into the faces of the local mesh  $\tau$ .

Given the above definition of the degrees of freedom on the local mesh we apply the mimetic finite difference (MFD) method from [?]. The method leads to the following system of equations with the matrix having the block structure:

$$\begin{pmatrix} \mathbf{M}_\tau & \mathbf{B}_\tau^T \\ -\mathbf{B}_\tau & \boldsymbol{\Sigma}_\tau \end{pmatrix} \begin{pmatrix} \mathbf{u}_\tau \\ \mathbf{p}_\tau \end{pmatrix} = \begin{pmatrix} \mathbf{E}_\tau \mathbf{C}_\tau \boldsymbol{\lambda}_\tau \\ \mathbf{f}_\tau \end{pmatrix}. \quad (6)$$

Here  $\mathbf{M}_\tau$ ,  $\boldsymbol{\Sigma}_\tau$ ,  $\mathbf{B}_\tau^T$ ,  $-\mathbf{B}_\tau$  are vector-mass, mass, gradient and divergence matrices, respectively;  $-\mathbf{C}_\tau$  is a diagonal scaling matrix with diagonal elements equal to the measures  $|f|$  of mini-faces  $f \in \mathbf{f}_{\text{ext}}(T)$ , i.e.  $-\mathbf{C}_\tau$  is the mass matrix for  $\boldsymbol{\lambda}_\tau$  unknowns;  $\mathbf{E}_\tau \in \mathbb{R}^{n_f \times n_\lambda}$  is a rectangular matrix with 0 and 1 entries which sparsifies a vector from  $\mathbb{R}^{n_\lambda}$  to a vector from  $\mathbb{R}^{n_f}$ . For the details on MFD and accurate definition of the matrices we refer to [?, ?]. Here we need the property that  $\mathbf{B}_\tau$  has a full row rank, and  $\mathbf{M}_\tau = \mathbf{M}_\tau^T$  is positive definite.

Since the continuity of flux condition (4) and boundary conditions are enforced on the *external* edges of  $T$ , we need to distinguish the vector  $\mathbf{u}_\tau^{\text{ext}}$  of fluxes on  $\mathbf{f}_{\text{ext}}(T)$ , which is just a trivial restriction of  $\mathbf{u}_\tau$  on the edges from  $\mathbf{f}_{\text{ext}}(T)$ ,

$$\mathbf{u}_\tau^{\text{ext}} := \mathbf{E}_\tau^T \mathbf{u}_\tau, \quad (7)$$

where  $\mathbf{E}_\tau^T$  is the restriction matrix with entries equal 0 or 1.

We now eliminate  $\mathbf{u}_\tau$  from (6) and express  $\mathbf{p}_\tau$  in terms of  $\boldsymbol{\lambda}_\tau$  (*static condensation*); recovering fluxes (backward substitution) and using (7) we get

$$\mathbf{u}_\tau^{\text{ext}} = \mathbf{A}_\tau \mathbf{C}_\tau \boldsymbol{\lambda}_\tau - \mathbf{a}_\tau, \quad (8)$$

with

$$\mathbf{A}_\tau = \mathbf{E}_\tau^T \left( \mathbf{M}_\tau^{-1} - \mathbf{M}_\tau^{-1} \mathbf{B}_\tau^T (\boldsymbol{\Sigma}_\tau + \mathbf{B}_\tau \mathbf{M}_\tau^{-1} \mathbf{B}_\tau^T)^{-1} \mathbf{B}_\tau \mathbf{M}_\tau^{-1} \right) \mathbf{E}_\tau, \quad (9)$$

$$\mathbf{a}_\tau = \mathbf{E}_\tau^T \mathbf{M}_\tau^{-1} \mathbf{B}_\tau^T (\boldsymbol{\Sigma}_\tau + \mathbf{B}_\tau \mathbf{M}_\tau^{-1} \mathbf{B}_\tau^T)^{-1} \mathbf{f}_\tau. \quad (10)$$

Note that matrices  $\mathbf{A}_\tau$  and vectors  $\mathbf{a}_\tau$  are computed locally for each  $T \in \mathcal{T}$ .

Next, we should use the continuity of flux condition (4) and boundary conditions to obtain a complete system for  $\mathbf{u}_\tau^{\text{ext}}$  and  $\boldsymbol{\lambda}_\tau$ . However, we cannot do this in a straightforward way, since the discontinuity of material interfaces across the macro-mesh faces may lead to a mismatch of discrete fluxes from two sides of  $F \in \mathcal{F}_{\text{int}}$ . [We elaborate on this below.](#)

For  $F \in \mathcal{F}_{\text{int}}$  shared by two polygonal cells  $T^\pm \in \mathcal{T}$  denote by  $\mathbf{f}_F(T^\pm) \subset \mathbf{f}_{\text{ext}}(T^\pm)$  the subsets of mini-faces that belong to the macro-face  $F$  from each side. In general,  $\mathbf{f}_F(T^+)$  and  $\mathbf{f}_F(T^-)$  may have a different number of mini-faces that make up the macro-face  $F$ , i.e.  $\#\mathbf{f}_F(T^+) \neq \#\mathbf{f}_F(T^-)$ , and hence the restrictions of concentration vectors  $\boldsymbol{\lambda}_\tau$  and fluxes vectors  $\mathbf{u}_\tau^{\text{ext}}$  can be of different sizes. Even if  $\#\mathbf{f}_F(T^+) = \#\mathbf{f}_F(T^-)$ , the locations of the mini-faces may be different due to volume- or moment-of-fluid interface reconstruction.

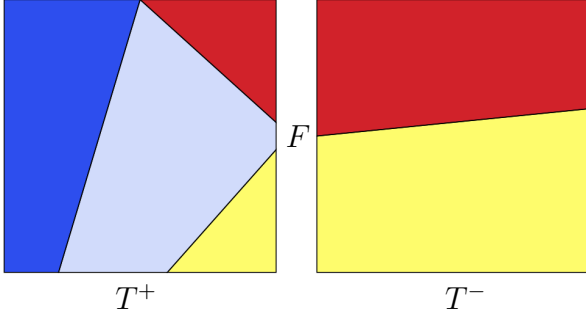


Figure 3: [Example of the mismatch of discrete fluxes from two sides of  \$F \in \mathcal{F}\_{\text{int}}\$](#)

See an example in Figure 3. We have  $3 = \#\mathbf{f}_F(T^+) \neq \#\mathbf{f}_F(T^-) = 2$ . Note also that locations of mini-faces corresponding to the same material are different from each side of  $F$ . This makes matching concentration and fluxes values not straightforward. Therefore, we shall enforce the flux continuity condition in the spirit of the mortar finite element method [?] using the space of functions defined on  $\mathcal{F}_{\text{int}}$ , which are polynomials of degree at most  $n$  on every  $F \in \mathcal{F}_{\text{int}}$ , an analog of the Lagrange multiplier space in the mortar method:

$$\Lambda = \{ \lambda \in \mathbb{L}^2(\mathcal{F}_{\text{int}}) : \lambda \in P_n \text{ for any } F \in \mathcal{F}_{\text{int}} \}.$$

When the Lagrange multiplier space  $\Lambda$  couples local MFD solutions, it is convenient to define degrees of freedom for  $\lambda \in \Lambda$  in terms of its  $(n+1)$  moments  $\lambda_F^{(i)}$  on every internal face  $F \in \mathcal{F}_{\text{int}}$ :

$$\lambda_F^{(i)} = \frac{\int_F \lambda s_i \, dl}{|F|}, \quad i = 0, \dots, n. \quad (11)$$

Here  $\{s_i\}_{i=0, \dots, n}$  is the set of  $\mathbb{L}^2(F)$ -orthogonal polynomials on  $F$  of degree  $n$ .

Let  $\nu_F := \max \{ \#\mathbf{f}_F(T^+), \#\mathbf{f}_F(T^-) \}$ . We set  $\mathcal{F}_T \subset \mathcal{F}$  to be the subset of macro-faces forming the boundary of a cell  $T$ . With each face  $F \in \mathcal{F}_T$  we associate  $\min \{ n+1, \nu_F \}$  degrees of freedom (11) in the  $\Lambda$  space. The local and global number of d.o.f. are

$$n_T := \sum_{F \in \mathcal{F}_T} \min \{ n+1, \nu_F \} \quad \text{and} \quad n_{\mathcal{T}} := \sum_{F \in \mathcal{F}} \min \{ n+1, \nu_F \},$$



respectively.

Further denote by  $\boldsymbol{\lambda}_T \in \mathbb{R}^{n_T}$  a vector of d.o.f. for elements of  $\Lambda$  associated with all macro-faces spanning the boundary of  $T$ . We need a correspondence between elements of  $\Lambda$  and local face elements  $\boldsymbol{\lambda}_\tau$  used as boundary data in local problem (6). This corresponding is given by the interpolation matrix  $\mathbf{R}_\tau$ ,

$$\boldsymbol{\lambda}_\tau = \mathbf{R}_\tau \boldsymbol{\lambda}_T, \quad (12)$$

where  $\boldsymbol{\lambda}_\tau$  is effectively a piecewise constant approximation of  $\boldsymbol{\lambda}_T$  on  $\mathbf{f}_{\text{ext}}(T)$ . Using this in (8), we get

$$\mathbf{u}_\tau^{\text{ext}} = \mathbf{A}_\tau \mathbf{C}_\tau \mathbf{R}_\tau \boldsymbol{\lambda}_T - \mathbf{a}_\tau. \quad (13)$$

If we find the mortar vector  $\boldsymbol{\lambda}_T$ , we recover the local approximation to the face concentration, i.e.  $\boldsymbol{\lambda}_\tau$ , from (12). Further we solve numerically local subproblems in (3) applying the mimetic FD method. This completes the solution algorithm for (1).

The dimension of the  $\Lambda$  space is  $n_\mathcal{F}$ , i.e.  $(n+1)$  or less unknowns for each face  $F \in \mathcal{F}$ . To obtain the system of  $n_\mathcal{F}$  equations, we enforce the weak continuity of the moments of fluxes on each internal macro-face

$$\int_F \mathbf{u}|_{T^+} \cdot \hat{\mathbf{n}} s_i \, dl = \int_F \mathbf{u}|_{T^-} \cdot \hat{\mathbf{n}} s_i \, dl, \quad i = 0, \dots, n, \quad \text{for each } F \in \mathcal{F}_{\text{int}}, \quad (14)$$

with  $(\mathbf{u}|_{T^+} \cdot \hat{\mathbf{n}})(\mathbf{x}) = u_\tau^{\text{ext}}(f)|f|$ , if  $\mathbf{x} \in f$  for  $f \in \mathbf{f}_F(T^+)$ , and  $u_\tau^{\text{ext}}(f)$  is the local flux assigned to  $f$  (component of  $\mathbf{u}_\tau^{\text{ext}}$ ). Similar definition applies to  $\mathbf{u}|_{T^-}$ . This and (13) result in the linear algebraic system

$$\mathbf{S}_\mathcal{F} \boldsymbol{\lambda}_\mathcal{F} = \mathbf{b}_\mathcal{F}, \quad (15)$$

with  $\mathbf{S}_\mathcal{F} \in \mathbb{R}^{n_\mathcal{F} \times n_\mathcal{F}}$ ,  $\boldsymbol{\lambda}_\mathcal{F}, \mathbf{b}_\mathcal{F} \in \mathbb{R}^{n_\mathcal{F}}$ . Neumann boundary condition in (2) is handled in the similar way, and Dirichlet boundary data in (2) is enforced strongly in (15).

Matrix  $\mathbf{S}_\mathcal{F}$  is sparse and its sparsity pattern does not depend on mini-meshes. Some useful properties of this matrix will be discussed in the next section.

### 3.1 Matrix properties

In this section we discuss the assembly procedure of the global matrix from (15) and show that  $\mathbf{S}_\mathcal{F}$  is symmetric positive definite. We concentrate on ASC(1), which we implement and validate in the next section. We shall make necessary remarks about ASC(0) as it is largely obtained by obvious simplifications of ASC(1).

The method uses local piecewise constant and global piecewise  $P_1$  (for ASC(1)) approximation of the concentration on  $\mathcal{F}$ . Local piecewise constant approximations  $\boldsymbol{\lambda}_\tau$ , however, use finer local subdivisions, so  $\boldsymbol{\lambda}_\tau$  does not belong to the restriction of the global space  $\Lambda$  on the boundary of a given cell  $T$ . For the method, we define a mapping given by the matrix  $\mathbf{R}_\tau$  to map global to local degrees of freedom and  $\mathbf{R}_\tau^T$  from local to global. For the well-posedness of the method, we need  $\mathbf{R}_\tau$  to have a full rank.

We define  $\mathbf{R}_\tau$  locally for any fixed  $T \in \mathcal{T}$ . Let us enumerate all faces of the given  $T$  by index  $j$ . For example,  $j = 1, \dots, 4$  for the polygonal cell in Figure 4. For each  $j$ , index  $i$  enumerates mini-faces from  $\mathbf{f}_{\text{ext}}(T)$  belonging to the macro-face  $j$ . For example,



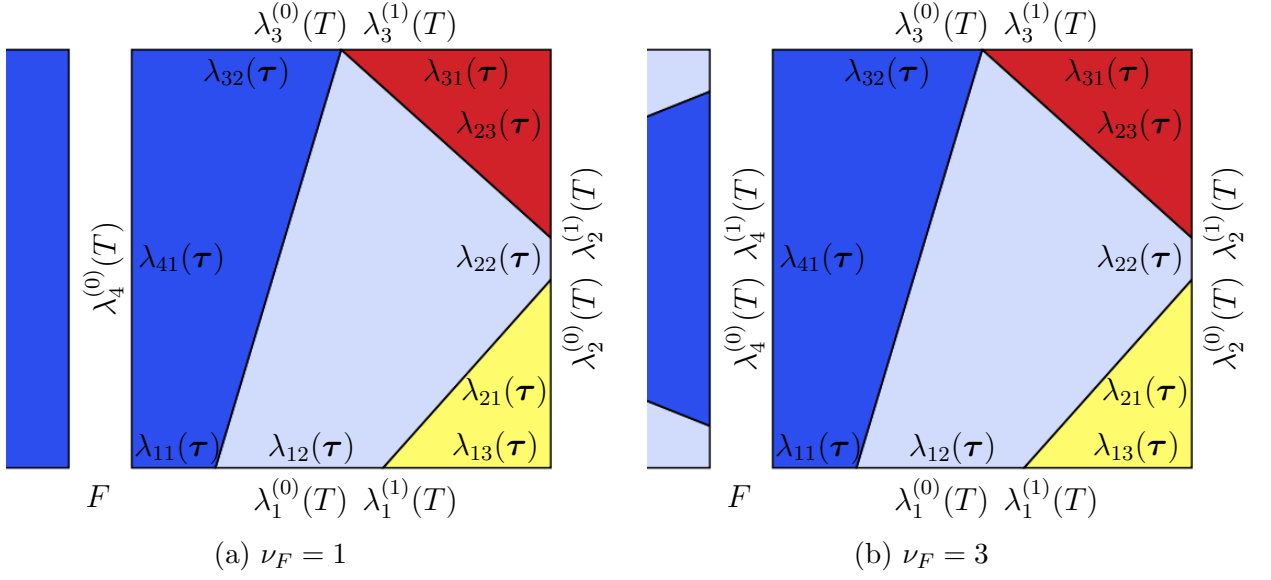


Figure 4:  $\lambda_{ji}(\boldsymbol{\tau})$  are local d.o.f. used in MFD for  $\lambda$  from (3),  $\lambda_j^{(0)}(T)$ ,  $\lambda_j^{(1)}(T)$  are global d.o.f. used to describe mortar space  $\Lambda$ . Left: Face  $F$  is single-material and uses one global d.o.f.; Right: Face  $F$  is multi-material and uses two global d.o.f.

$i \in \{1, 2, 3\}$  for  $j = 1$  and  $i \in \{1\}$  for  $j = 4$  for the same example in Figure 4. Further, denote by  $\lambda_{ji}(\boldsymbol{\tau})$  the local d.o.f. assigned to the  $i$ -th mini-face belonging to the  $j$ -th macro-face, and by  $\lambda_j^{(0)}(T)$ ,  $\lambda_j^{(1)}(T)$  two moments defining an element from  $\Lambda$  on the  $j$ -th macro-face (see Figure 4) so that we have

$$\lambda(\mathbf{r}(t)) = \lambda_j^{(1)}(T) |F| t + \left( \lambda_j^{(0)}(T) - \frac{\lambda_j^{(1)}(T) |F|}{2} \right), \quad F \in \mathcal{F}_{\text{int}} \quad (16)$$

for  $\lambda \in \Lambda$ . Here  $t \in (0, 1)$  and  $\mathbf{r} : (0, 1) \rightarrow F$  is the affine parametrization of the face  $F$  with index  $j$  among macro-faces of  $T$ .

Integrating (16) over all mini-faces  $f \in \mathbf{f}_F(T)$  ( $f$  has local index  $i$  among mini-faces belonging to  $F$ ) and re-scaling, we get

$$\lambda_{ji}(\boldsymbol{\tau}) = \begin{cases} \lambda_j^{(0)}(T) + s_{ji} \lambda_j^{(1)}(T), & \text{if } F \text{ is a multi-material face,} \\ \lambda_j^{(0)}(T), & \text{otherwise,} \end{cases} \quad (17)$$

where  $s_{ji} \equiv s_f$  is a signed distance between centroids of  $f$  and  $F$ , i.e. if  $\mathbf{a}_F$ ,  $\mathbf{b}_F$  and  $\mathbf{a}_f$ ,  $\mathbf{b}_f$  are vertices forming macro-face  $F$  and mini-face  $f$ , respectively, then we have

$$s_f := \left\| \frac{\mathbf{a}_f + \mathbf{b}_f}{2} - \mathbf{a}_F \right\|_2 - \left\| \frac{\mathbf{a}_F + \mathbf{b}_F}{2} - \mathbf{a}_F \right\|_2. \quad (18)$$

For the corresponding vectors of unknowns  $\boldsymbol{\lambda}_{\boldsymbol{\tau}} = \{\lambda_{ji}(\boldsymbol{\tau})\}$  and  $\boldsymbol{\lambda}_T = \{\lambda_j^{(0)}(T)\} \cup \{\lambda_j^{(1)}(T)\}$  equation (17) defines the matrix  $\mathbf{R}_{\boldsymbol{\tau}}$  through (12). For the example in Figure 4 (left and

right) we have

$$\mathbf{R}_\tau = \begin{pmatrix} 1 & s_{11} & 0 & 0 & 0 & 0 & 0 \\ 1 & s_{12} & 0 & 0 & 0 & 0 & 0 \\ 1 & s_{13} & 0 & 0 & 0 & 0 & 0 \\ 0 & 0 & 1 & s_{21} & 0 & 0 & 0 \\ 0 & 0 & 1 & s_{22} & 0 & 0 & 0 \\ 0 & 0 & 1 & s_{23} & 0 & 0 & 0 \\ 0 & 0 & 0 & 0 & 1 & s_{31} & 0 \\ 0 & 0 & 0 & 0 & 1 & s_{32} & 0 \\ 0 & 0 & 0 & 0 & 0 & 0 & 1 \end{pmatrix}, \quad \lambda_\tau = \begin{pmatrix} \lambda_{11}(\tau) \\ \lambda_{12}(\tau) \\ \lambda_{13}(\tau) \\ \lambda_{21}(\tau) \\ \lambda_{22}(\tau) \\ \lambda_{23}(\tau) \\ \lambda_{31}(\tau) \\ \lambda_{32}(\tau) \\ \lambda_{41}(\tau) \end{pmatrix};$$

for the moment d.o.f. we have

$$\lambda_T = \left( \lambda_1^{(0)}(T), \lambda_1^{(1)}(T), \lambda_2^{(0)}(T), \lambda_2^{(1)}(T), \lambda_3^{(0)}(T), \lambda_3^{(1)}(T), \lambda_4^{(0)}(T) \right)^T \text{ and} \\ \left( \lambda_1^{(0)}(T), \lambda_1^{(1)}(T), \lambda_2^{(0)}(T), \lambda_2^{(1)}(T), \lambda_3^{(0)}(T), \lambda_3^{(1)}(T), \lambda_4^{(0)}(T), \lambda_4^{(1)}(T) \right)^T$$

for Figure 4 (left) and Figure 4 (right), respectively. For ASC(0) the matrix  $\mathbf{R}_\tau$  is as above with rows containing  $s_{ij}$ -s eliminated.

Now, when the mappings between local and global approximations of  $\lambda$  are defined, we are ready to proceed with the assembly of the global matrix  $\mathbf{S}_\mathcal{T}$ . The flux continuity over the face  $F$  (condition (14)) yields

$$\begin{cases} \sum_{f \in f_F(T^+)} u_{\tau^+}^{\text{ext}}(f) |f| + \sum_{f \in f_F(T^-)} u_{\tau^-}^{\text{ext}}(f) |f| = 0, \\ \sum_{f \in f_F(T^+)} u_{\tau^+}^{\text{ext}}(f) \int_f s_1 \, dl + \sum_{f \in f_F(T^-)} u_{\tau^-}^{\text{ext}}(f) \int_f s_1 \, dl = 0. \end{cases} \quad (19)$$

Integrating the first moments in the second equation of (19), one gets

$$\sum_{f \in f_F(T^+)} u_{\tau^+}^{\text{ext}}(f) s_f |f| + \sum_{f \in f_F(T^-)} u_{\tau^-}^{\text{ext}}(f) s_f |f| = 0,$$

where  $s_f$  is defined in (18). Noting that matrix  $\mathbf{C}_\tau$  from (6) has mini-faces' measures on its diagonal, and interpolation matrix  $\mathbf{R}_\tau$  defined via (17) has signed distances and ones as its elements, one can rewrite (19) in the matrix form

$$(\mathbf{R}_{\tau^+}^T \mathbf{C}_{\tau^+} \mathbf{u}_{\tau^+}^{\text{ext}})_{i+m} + (\mathbf{R}_{\tau^-}^T \mathbf{C}_{\tau^-} \mathbf{u}_{\tau^-}^{\text{ext}})_{j+m} = 0, \quad m \in \{0, 1\} \quad (20)$$

where  $i$  and  $j$  are the local indexes of the face  $F$  in the cells  $T^+$  and  $T^-$ , respectively ( $m = 0$  corresponds to the first equation in (19) and  $m = 1$  corresponds to the second one; further we omit “+ $m$ ” for simplicity). For the Neumann part of the boundary of  $T^\pm$  we set  $f_N(T^\pm) := \{f \in f_{\text{ext}}(T^\pm) : f \subset \partial\Omega_N\}$ . If  $F$  from  $T^+$  belongs to the Neumann part of the boundary, then we have

$$(\mathbf{R}_{\tau^+}^T \mathbf{C}_{\tau^+} \mathbf{u}_{\tau^+}^{\text{ext}})_i = (\mathbf{R}_{\tau^+}^T \mathbf{C}_{\tau^+} \mathbf{g}_{N\tau^+})_i, \quad \mathbf{g}_{N\tau^+} := \left\{ \int_f g_N s_m \, dl / |f| \right\}_{f \in f_N(T^+), m \in \{0, 1\}}.$$

Substituting (13) into (20) we get the local equation for  $\lambda_T$

$$\begin{aligned} \underbrace{\left( (\mathbf{R}_{\tau^+}^T \mathbf{C}_{\tau^+} \mathbf{A}_{\tau^+} \mathbf{C}_{\tau^+} \mathbf{R}_{\tau^+}) \lambda_{T^+} \right)}_{\mathbf{S}_{T^+} :=} \Big|_i + \underbrace{\left( (\mathbf{R}_{\tau^-}^T \mathbf{C}_{\tau^-} \mathbf{A}_{\tau^-} \mathbf{C}_{\tau^-} \mathbf{R}_{\tau^-}) \lambda_{T^-} \right)}_{\mathbf{S}_{T^-} :=} \Big|_j = \\ \underbrace{\left( \mathbf{R}_{\tau^+}^T \mathbf{C}_{\tau^+} \mathbf{a}_{\tau^+} \right)}_{\mathbf{b}_{T^+} :=} \Big|_i + \underbrace{\left( \mathbf{R}_{\tau^-}^T \mathbf{C}_{\tau^-} \mathbf{a}_{\tau^-} \right)}_{\mathbf{b}_{T^-} :=} \Big|_j. \end{aligned} \quad (21)$$

As standard in finite element methods, one assembles the global system (15) from the local matrices and local right-hand side vectors. Thus we may formally write

$$\mathbf{S}_{\mathcal{T}} = \sum_{T \in \mathcal{T}} \mathbf{N}_T^T \mathbf{S}_T \mathbf{N}_T, \quad \mathbf{b}_{\mathcal{T}} = \sum_{T \in \mathcal{T}} \mathbf{N}_T^T \mathbf{b}_T, \quad (22)$$

where  $\mathbf{N}_T$  defines global to local mapping for the cell  $T$ .

From (21) it is clear that  $\mathbf{S}_{\mathcal{T}}$  is sparse: Global d.o.f.  $\lambda_m^{(0)}(\mathcal{T})$ ,  $\lambda_m^{(1)}(\mathcal{T})$  (components of  $\lambda_{\mathcal{T}}$ ) interact only with d.o.f. associated with faces of macro-cells that share  $m$ th macro-face. For example, if  $F \in \mathcal{F}_{\text{int}}$  is shared by two quadrilaterals and has global index  $m$ , then  $m$ th row of  $\mathbf{S}_{\mathcal{T}}$  has at most 14 nonzero elements for ASC(1) and at most 7 for ASC(0).

Now we show that the global matrix  $\mathbf{S}_{\mathcal{T}}$  in (15) is symmetric and positive definite. We give the arguments for ASC(1). Same arguments hold for ASC(0) after obvious simplifications.

**Lemma 3.1.**  $\ker \mathbf{R}_{\tau} = \{\mathbf{0}\}$  for ASC(1)

*Proof.* From (17) we have that for any cell  $T$  and its mini-mesh  $\tau(T)$  the interpolating matrix may be written as

$$\mathbf{R}_{\tau} = \begin{pmatrix} \mathbf{S}_1 & & & \\ & \mathbf{S}_2 & & \\ & & \ddots & \\ & & & \mathbf{S}_m \end{pmatrix}, \quad (23)$$

where  $m :=$  number of macro-faces spanning  $\partial T$  and

$$\mathbf{S}_k := \begin{cases} \begin{pmatrix} 1 & s_{k1} \\ \vdots & \vdots \\ 1 & s_{km_k} \end{pmatrix}, & \text{if } k\text{th face is multi-material face,} \\ 1, & \text{otherwise,} \end{cases}$$

$1 < m_k$  is the number of mini-faces of the  $k$ th macro-face,  $s_{ki}$  is the signed distance between centroids of  $i$ th mini-face and  $k$ th macro-face. If  $T$  contains only one material, then  $\mathbf{R}_{\tau} = \mathbf{I}$  and hence  $\ker \mathbf{R}_{\tau} = \{\mathbf{0}\}$ , so we assume that there is at least one multi-material face.

Clearly, matrix  $\mathbf{R}_{\tau}$  has a non-trivial kernel iff

$$s_{ki} = s_{kj}, \quad i, j = 1, 2, \dots, m_k$$

for some  $k$ . Take some  $\mathbf{S} = \mathbf{S}_k$  corresponding to a multi-material face  $F \in \mathcal{F}_T$  with  $l := m_k$  materials,

$$\mathbf{S} = \begin{pmatrix} 1 & s_1 \\ \vdots & \vdots \\ 1 & s_l \end{pmatrix}.$$

It is sufficient to show that  $s_1 \neq s_2$ . Let  $f_1$  and  $f_2$  be corresponding mini-faces. We have

$$s_1 = \frac{1}{2} (|f_1| - |F|), \quad s_2 = |f_1| + \frac{1}{2} (|f_2| - |F|),$$

and

$$s_1 = s_2 \quad \Leftrightarrow \quad |f_1| + |f_2| = 0.$$

Hence  $s_1 \neq s_2$ , and  $\ker \mathbf{R}_\tau = \{\mathbf{0}\}$  follows.  $\square$

**Theorem 3.2.** *Matrix  $\mathbf{S}_\mathcal{T}$  is symmetric. If  $c > 0$  or  $|\partial\Omega_D| > 0$ , then  $\mathbf{S}_\mathcal{T}$  is positive definite.*

*Proof.* First, noting that for any two symmetric positive definite matrices  $\mathbf{A}_1$  and  $\mathbf{A}_2$  inequality  $\mathbf{A}_1 \geq \mathbf{A}_2$  implies  $\mathbf{A}_1^{-1} \leq \mathbf{A}_2^{-1}$ , we conclude

$$\tilde{\mathbf{B}}^T \left( \boldsymbol{\Sigma} + \tilde{\mathbf{B}} \tilde{\mathbf{B}}^T \right)^{-1} \tilde{\mathbf{B}} \leq \tilde{\mathbf{B}}^T \left( \tilde{\mathbf{B}} \tilde{\mathbf{B}}^T \right)^{-1} \tilde{\mathbf{B}} \leq \mathbf{I}, \quad (24)$$

where  $\boldsymbol{\Sigma}$  is any symmetric and non-negative definite matrix,  $\tilde{\mathbf{B}}$  is any matrix such that  $\ker \tilde{\mathbf{B}}^T = \{\mathbf{0}\}$ , and  $\mathbf{I}$  is identity matrix. To check the last inequality in (24), one can consider, e.g., the SVD decomposition of  $\tilde{\mathbf{B}}$ .

From the identities (9) and (24) with  $\tilde{\mathbf{B}}^T := \mathbf{M}_\tau^{-\frac{1}{2}} \mathbf{B}_\tau^T$ ,  $\boldsymbol{\Sigma} := \boldsymbol{\Sigma}_\tau$  it immediately follows that  $\mathbf{A}_\tau$  is symmetric and non-negative definite. The symmetry of  $\mathbf{S}_\mathcal{T}$  follows from the definition in (21)–(22). By similar considerations, it is easy to see that  $\mathbf{A}_\tau$  is positive definite for all  $T$ , where  $c > 0$ . Hence if  $c > 0$  in  $\Omega$ , then (21)–(22) and the full ranks of  $\mathbf{R}_\tau$ 's and  $\mathbf{C}_\tau$ 's imply the positive definiteness of  $\mathbf{S}_\mathcal{T}$ .

Now we show the positive definiteness of  $\mathbf{S}_\mathcal{T}$  if  $|\partial\Omega_D| > 0$ . Consider any given  $T \in \mathcal{T}$ . Matrix  $\mathbf{A}_\tau$  defines the discrete Dirichlet-to-Neumann map for  $\partial T$ . If  $\partial T \cap \partial\Omega_D$ , then  $\ker \mathbf{A}_\tau = \{\mathbf{0}\}$ . Otherwise  $\dim(\ker \mathbf{A}_\tau) = 1$  and  $\mathbf{A}_\tau \mathbf{C}_\tau \boldsymbol{\lambda}_\tau = \mathbf{0}$  implies that  $\boldsymbol{\lambda}_\tau$  is constant on  $\partial T$ . Consider some  $\lambda$  from the mortar space  $\Lambda$  and corresponding vector of moments  $\boldsymbol{\lambda}_\mathcal{T}$ . Using connectivity of the mesh one easily finds that  $\mathbf{R}_\tau \boldsymbol{\lambda}_T$  can be constant on every  $T \in \mathcal{T}$  only if  $\lambda$  is constant. Due to the assumption  $|\partial\Omega_D| > 0$  this implies  $\lambda = 0$ . Hence for any  $\mathbf{0} \neq \boldsymbol{\lambda}_\mathcal{T} \in \mathbb{R}^{n_\mathcal{T}}$  we have

$$\begin{aligned} (\mathbf{S}_\mathcal{T} \boldsymbol{\lambda}_\mathcal{T}, \boldsymbol{\lambda}_\mathcal{T}) &\stackrel{(22)}{=} \left( \left( \sum_{T \in \mathcal{T}} \mathbf{N}_T^T \mathbf{S}_T \mathbf{N}_T \right) \boldsymbol{\lambda}_\mathcal{T}, \boldsymbol{\lambda}_\mathcal{T} \right) = \sum_{T \in \mathcal{T}} (\mathbf{S}_T \mathbf{N}_T \boldsymbol{\lambda}_\mathcal{T}, \underbrace{\mathbf{N}_T \boldsymbol{\lambda}_\mathcal{T}}_{\boldsymbol{\lambda}_T}) \\ &= \sum_{T \in \mathcal{T}} (\mathbf{S}_T \boldsymbol{\lambda}_T, \boldsymbol{\lambda}_T) > 0. \end{aligned}$$

The last inequality holds, since there exists  $T$  such that  $\boldsymbol{\lambda}_T = \mathbf{N}_T \boldsymbol{\lambda}_\mathcal{T}$  is not in the kernel for  $\boldsymbol{\lambda}_\mathcal{T} \neq \mathbf{0}$ .  $\square$

## 4 Numerical results

Let  $h$  be a maximum cell diameter for the macro-mesh  $\mathcal{T}_h$ , and  $\mathbb{V}_h \subset \mathbb{L}^2(\Omega)$  be a space of piecewise constant functions on each cell  $\tau \in \boldsymbol{\tau}(T)$ ,  $T \in \mathcal{T}_h$ . For  $v \in \mathbb{L}^2(\Omega)$  we define

$$\|v\|_{\ell^2(\Omega)} := \|P_h v\|_{\mathbb{L}^2(\Omega)}, \quad (25)$$

where  $P_h : \mathbb{L}^2(\Omega) \rightarrow \mathbb{V}_h$  is  $\mathbb{L}^2$ -projection operator. Note that  $\|\cdot\|_{\ell^2(\Omega)}$  defines a norm in  $\mathbb{V}_h$ ; we will refer to it as *discrete*  $\mathbb{L}^2$ -norm.

For the error  $e_h := p - p_h$  between the exact and computed solutions we have

$$e_h^{\ell^2} := \|e_h\|_{\ell^2(\Omega)} = \|p - p_h\|_{\ell^2(\Omega)} = \|P_h p - P_h p_h\|_{\mathbb{L}^2(\Omega)} = \|P_h p - p_h\|_{\mathbb{L}^2(\Omega)} \quad (26)$$

since  $P_h$  is linear and  $p_h \in \mathbb{V}_h$ . This gives

$$e_h^{\ell^2} = \left[ \sum_{T \in \mathcal{T}_h} \sum_{\tau \in \boldsymbol{\tau}(T)} \left( \frac{1}{|\tau|} \int_{\tau} p \, d\mathbf{x} - p_h(\tau) \right)^2 |\tau| \right]^{\frac{1}{2}},$$

where  $|\tau|$  is the area of cell  $\tau$ . The discrete norm of the flux discretization error is defined as follows:

$$\varepsilon_h^{l_2} = \left[ \sum_{F \in \mathcal{F}} A_F \left( \sum_{f \in F} \frac{1}{|f|} \int_f \mathbf{u} \, d\mathbf{s} - \sum_{f \in F} \mathbf{u}_h(f) \right)^2 \right]^{\frac{1}{2}}$$

where  $A_F$  is the reference volume of a face  $F$  which is equal to the arithmetic average of volumes of cells sharing the face  $F$ .

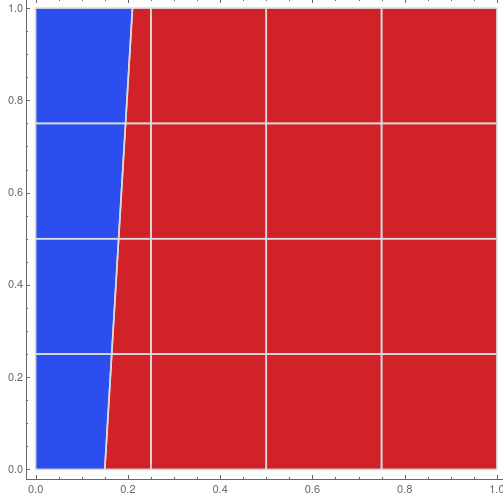
If  $\mathcal{T}_h$  consists of triangles and *no* material interfaces are present, ASC( $n$ ) reduces to mixed-hybrid Raviart–Thomas finite element method (which is algebraically equivalent to  $RT_0$  finite element method). In this particular case we have [?]

$$\|\mathbf{u} - \mathbf{u}_h\|_{\mathbb{L}^2(\Omega)} \leq c h \|\mathbf{u}\|_{\mathbb{H}^1(\Omega)}, \quad \|p - p_h\|_{\mathbb{L}^2(\Omega)} \leq c (h \|p\|_{\mathbb{H}^1(\Omega)} + h^2 \|p\|_{\mathbb{H}^2(\Omega)}),$$

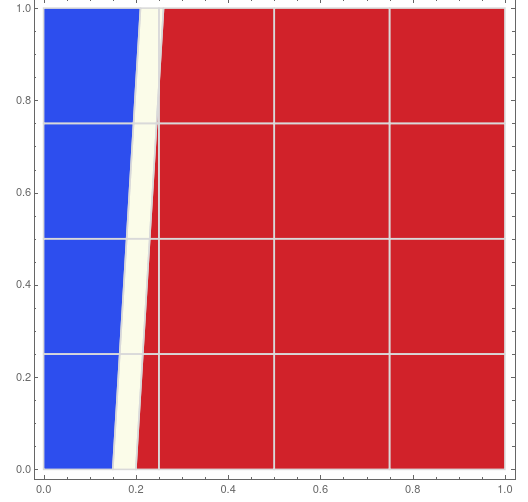
so one should not expect ASC( $n$ )  $\mathbb{L}^2$ -convergence to be better than linear. However, since we measure convergence of the averages values and  $\|p - p_h\|_{\ell^2(\Omega)} \leq \|p - p_h\|_{\mathbb{L}^2(\Omega)}$  by the property of projection, we may observe a higher order convergence for smooth solutions.

### 4.1 Linear solution

The first set of tests is designed to check the property of the method to accurately recover the solution that given by a polynomial of degree 1. Let us consider the diffusion problem (1) with  $c \equiv f \equiv 0$ ,  $\partial\Omega_D = \partial\Omega$ . The computational domain  $\Omega = (0, 1)^2$  is divided into several subdomains by non-intersecting straight lines. In these settings the interface reconstruction algorithm MOF reconstructs the interfaces exactly. To test this preservation property, we set up a pseudo-multi-material problem with the diffusion tensor being the same in all subdomains,  $\mathbf{K}_i = \mathbf{I}$ . The exact solution is a linear function. The geometry of two cases under consideration is shown in Figure 5.



(a)  $\mathbf{K}_1 \equiv \mathbf{K}_2 \equiv \mathbf{I}$



(b)  $\mathbf{K}_1 \equiv \mathbf{K}_2 \equiv \mathbf{K}_3 \equiv \mathbf{I}$

Figure 5: Material distribution for pseudo-multi-material problem: two materials (left), three materials (right)

We denote the solution computed with the ASC( $n$ ) method by  $p_{h,n}$ ,  $n = 0, 1$ . For ASC(0) we have  $e_{h,0}^{\ell^2} = 6.38 \times 10^{-2}$  and  $6.41 \times 10^{-2}$  for the configurations shown in Figures 5a and 5b, respectively. That is, ASC(0) is not able to recover  $P_1$  solutions exactly.

Since ASC(1) approximates interface traces with  $P_1$  functions it recovers edge-based degrees of freedom exactly in the sense of mean values. This results in exact reconstruction of cell-based unknowns and the preservation property holds for both examples, i.e.

$$e_{h,1}^{\ell^2} = \|p - p_{h,1}\|_{\ell^2(\Omega)} = 0.$$

## 4.2 Piecewise $P_1$ solution

In this set of tests, we consider the diffusion problem (1) with  $c \equiv f \equiv 0$ ,  $\partial\Omega_D = \partial\Omega$ , and two different materials in the domain.  $\mathbf{K} = k\mathbf{I}$ ,  $k = 1$  in the left part of the domain and  $k = 0.1$  in the right (see Figure 6b). The exact solution is piecewise linear such that the normal flux is continuous across the interface (see Figure 6a).

For this example we use a sequence of square base meshes  $\mathcal{T}_{h_i}$ ,  $i = 1, 2, 3, 4$ . We denote by

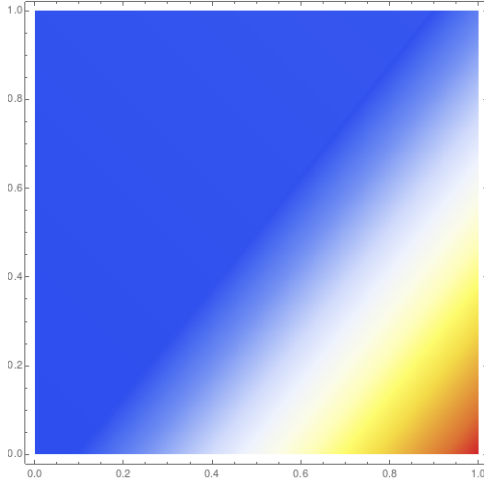
$$\rho_{h_i,n} := \frac{\ln(e_{h_i,n}^{\ell^2}/e_{h_{i+1},n}^{\ell^2})}{\ln(h_i/h_{i+1})}$$

the convergence order of ASC( $n$ ) in  $\ell^2$ -norm between  $i$ th and  $(i+1)$ th refinement steps. We also compute the  $\ell^\infty$ -norm of the error

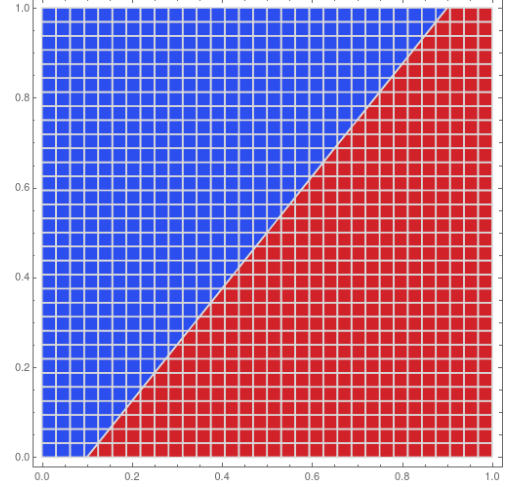
$$e_{h_i,n}^\infty := \|p - p_{h_i,n}\|_\infty$$

for ASC( $n$ ).

Numerical results are shown in Table 1. We see that ASC(0) converges linearly with respect to the  $\ell^2$ -norm, and ASC(1) has the convergence rate close to quadratic with respect to the same norm. The convergence of the flux errors is also higher for ASC(1) method and is close to linear convergence.



(a) Reference solution  $p$



(b) Materials:  $k_1 = 1$ ,  $k_2 = 0.1$

Figure 6: Piecewise linear reference solution

Table 1: Piecewise linear example: convergence

ASC(0)	$h$	$e_0^{\ell^2}$	$\rho_p$	$e_0^\infty$	$\varepsilon_0^{l_2}$	$\rho_u$
	$3.5 \times 10^{-1}$	$7.3 \times 10^{-1}$		4.8	$6.6 \times 10^{-1}$	
	$8.8 \times 10^{-2}$	$1.6 \times 10^{-1}$	1.1	1.2	$3.5 \times 10^{-1}$	0.46
	$2.2 \times 10^{-2}$	$3.7 \times 10^{-2}$	1.1	$3.4 \times 10^{-1}$	$1.3 \times 10^{-1}$	0.71
	$5.5 \times 10^{-3}$	$8.9 \times 10^{-3}$	1.0	$7.9 \times 10^{-2}$	$4.1 \times 10^{-2}$	0.83
ASC(1)	$h$	$e_1^{\ell^2}$	$\rho_p$	$e_1^\infty$	$\varepsilon_1^{l_2}$	$\rho_u$
	$3.5 \times 10^{-1}$	$2.5 \times 10^{-2}$		$2.9 \times 10^{-1}$	$4.6 \times 10^{-2}$	
	$8.8 \times 10^{-2}$	$1.9 \times 10^{-3}$	1.84	$6.6 \times 10^{-2}$	$2.0 \times 10^{-2}$	0.6
	$2.2 \times 10^{-2}$	$1.6 \times 10^{-4}$	1.79	$4.3 \times 10^{-2}$	$5.5 \times 10^{-3}$	0.93
	$5.5 \times 10^{-3}$	$1.3 \times 10^{-5}$	1.80	$2.0 \times 10^{-2}$	$1.3 \times 10^{-3}$	1.

## 4.3 Piecewise $P_2$ solutions

### 4.3.1 Two materials

Let us consider the diffusion problem (1) with  $c \equiv 0$ ,  $\partial\Omega_D = \partial\Omega$ . The computational domain is divided into subdomains:  $\Omega_1 = \{\mathbf{x} : \|\mathbf{x} - \mathbf{x}_0\| < 0.2\}$  with  $\mathbf{x}_0 = (0.5, 0.5)$  and  $\Omega_2 = (0, 1)^2 \setminus \bar{\Omega}_1$ . The diffusion tensor is set to be  $\mathbf{K}_i = k_i \mathbf{I}$  in  $\Omega_i$ ,  $k_1 = 0.001$  and  $k_2 = 1$ . The exact solution is piecewise quadratic such that the normal flux is continuous across the interface (see Figure 7). For this problem we compare convergence properties of the ASC(0) and ASC(1) methods on a sequence of Voronoi meshes.

The norms of the errors are shown in Table 2. ASC(1) demonstrates convergence with the rate in the  $\ell^2$ -norm close to quadratic for scalar unknowns and even higher than linear for flux errors. **It is important to take into account** that approximation errors in the interface reconstruction may effect the convergence of discretization methods. For example, in these set of tests ASC(0) convergence rate fluctuates significantly for both



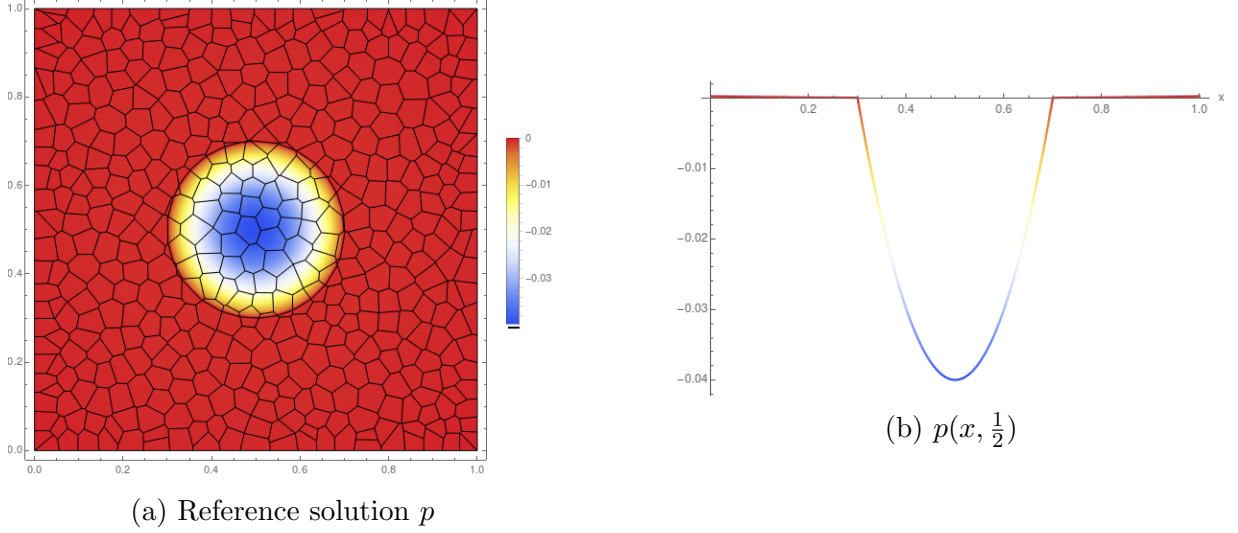


Figure 7: Piecewise quadratic reference solution, 2 materials

Table 2: Piecewise quadratic example, two materials: convergence

ASC(0)	$h$	$e_0^{\ell^2}$	$\rho_p$	$e_0^\infty$	$\varepsilon_0^{l^2}$	$\rho_u$
	$3.0 \times 10^{-1}$	$2.4 \times 10^{-3}$		$6.3 \times 10^{-1}$	$6.9 \times 10^{-5}$	
	$1.5 \times 10^{-1}$	$6.5 \times 10^{-4}$	2.0	$7.0 \times 10^{-3}$	$3.6 \times 10^{-5}$	0.9
	$8.1 \times 10^{-2}$	$2.6 \times 10^{-4}$	1.4	$3.2 \times 10^{-3}$	$3.4 \times 10^{-5}$	0.09
	$4.2 \times 10^{-2}$	$1.4 \times 10^{-4}$	0.9	$2.3 \times 10^{-3}$	$2.1 \times 10^{-5}$	0.73
	$2.1 \times 10^{-2}$	$3.7 \times 10^{-5}$	1.9	$1.1 \times 10^{-3}$	$1.1 \times 10^{-5}$	0.93
	$1.0 \times 10^{-2}$	$2.7 \times 10^{-5}$	0.4	$8.6 \times 10^{-4}$	$6.5 \times 10^{-6}$	0.75
ASC(1)	$h$	$e_1^{\ell^2}$	$\rho_p$	$e_1^\infty$	$\varepsilon_1^{l^2}$	$\rho_u$
	$3.0 \times 10^{-1}$	$2.4 \times 10^{-3}$		$2.1 \times 10^{-3}$	$1.2 \times 10^{-4}$	
	$1.5 \times 10^{-1}$	$7.0 \times 10^{-4}$	1.9	$1.3 \times 10^{-2}$	$6.5 \times 10^{-5}$	0.88
	$8.1 \times 10^{-2}$	$2.3 \times 10^{-4}$	1.8	$6.8 \times 10^{-4}$	$3.0 \times 10^{-5}$	1.25
	$4.2 \times 10^{-2}$	$6.8 \times 10^{-5}$	1.8	$3.2 \times 10^{-4}$	$1.4 \times 10^{-5}$	1.16
	$2.1 \times 10^{-2}$	$2.0 \times 10^{-5}$	1.8	$1.1 \times 10^{-4}$	$5.0 \times 10^{-6}$	1.48
	$1.0 \times 10^{-2}$	$5.4 \times 10^{-6}$	1.9	$3.3 \times 10^{-5}$	$2.2 \times 10^{-6}$	1.18

scalar and flux errors. We also observe a bump in the max norm error for ASC(1) on the second mesh level,  $h = 1.5 \times 10^{-1}$ . To have some insight, we show the corresponding mesh in the Figure 8a. One may note that the interface reconstruction produces significant discontinuity of interfaces: A small volume of the external material, i.e. the one occupying  $\Omega_2$  domain, appears inside the disk (domain  $\Omega_1$ ). Due to constant trace approximation, ASC(0) is not sensitive to such irregularity. It turns out that for ASC(1) the  $\ell^\infty$  norm of the error is affected by the appearance of such small isolated cut cells. At the same time, this does not affect the  $\ell^2$ -convergence of ASC(1).

### 4.3.2 Three materials

In the next group of numerical tests, we consider the same diffusion problem (1) with  $c \equiv 0$ ,  $\partial\Omega_D = \partial\Omega$ . The computational domain is now divided into three subdomains:  $\Omega_1 = \{\mathbf{x} : \|\mathbf{x} - \mathbf{x}_0\| < 0.15\}$ ,  $\Omega_2 = \{\mathbf{x} : 0.15 < \|\mathbf{x} - \mathbf{x}_0\| < 0.2\}$ , and  $\Omega_3 = (0, 1)^2 \setminus (\bar{\Omega}_1 \cup \bar{\Omega}_2)$ .

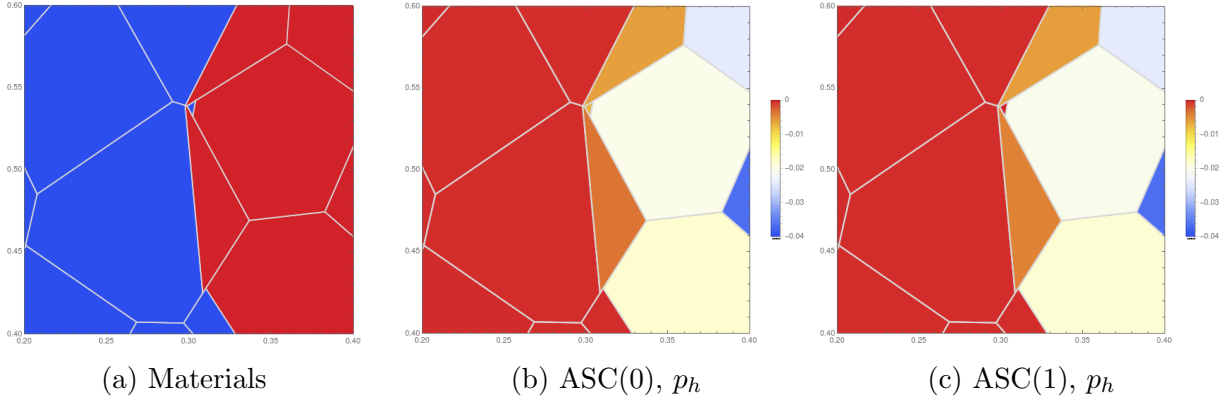


Figure 8: Piecewise quadratic example, two materials:  $h = 1.5 \times 10^{-1}$ . This figure illustrates the appearance of small isolated material volumes during numerical reconstruction of material interfaces. This may affect the  $\ell^\infty$  error norm of the ASC(1)

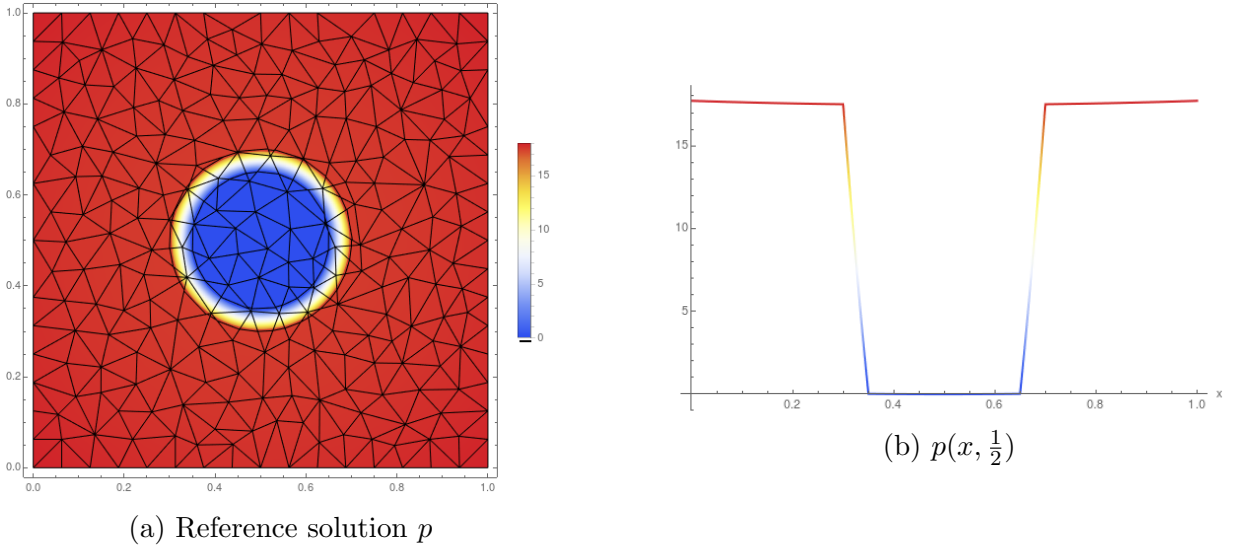


Figure 9: Piecewise quadratic reference solution, three materials

The diffusion tensor is set to be  $\mathbf{K}_i = k_i \mathbf{I}$ ,  $k_1 = k_3 = 1$ ,  $k_2 = 0.001$ . The geometry represents a ring with  $k_2 = 0.001$  inside the ring and  $k_1 = k_3 = 1$  outside the ring. The exact solution is piecewise quadratic such that the normal flux is continuous across the interface; see Figure 9. We use a sequence of triangular meshes to study convergence for this example. In this set of tests, we also consider the numerical method based on homogenization techniques for the comparison. The homogenization method we use is from [?]. The homogenized values of the diffusion tensor are computed on the base cells  $T$  and then plugged into the MFD discretization applied on the base mesh  $\mathcal{T}_h$ ; see [?] for implementation details of this method.

Numerical results are shown in Table 3. We compare ASC(0), ASC(1), arithmetic, and harmonic homogenization. Note that up to mesh level  $h = 8.3 \times 10^{-2}$  macro-faces with three materials are present, and starting from  $h = 6.7 \times 10^{-2}$  the meshes are fine enough so that only macro-faces sharing one or two materials occur.

Table 3: Piecewise quadratic example, three materials: error norms and convergence rates

ASC(0)	$h$	$e_0^{\ell^2}$	$\rho$	$e_0^\infty$
	$3.0 \times 10^{-1}$	4.5		17
	$2.5 \times 10^{-1}$	4.5		17
	$1.3 \times 10^{-1}$	4.0		17
	$8.3 \times 10^{-2}$	4.4		17
	$6.7 \times 10^{-2}$	$7.1 \times 10^{-1}$		4.9
	$4.3 \times 10^{-2}$	$4.5 \times 10^{-1}$	1.2	5.0
ASC(1)	$h$	$e_0^{\ell^2}$	$\rho$	$e_0^\infty$
	$3.0 \times 10^{-1}$	$4.5 \times 10^{-1}$		3.5
	$2.5 \times 10^{-1}$	$2.6 \times 10^{-1}$	3	2.7
	$1.3 \times 10^{-1}$	$9.2 \times 10^{-2}$	1.5	$6.2 \times 10^{-1}$
	$8.3 \times 10^{-2}$	$4.8 \times 10^{-2}$	1.6	$8.3 \times 10^{-1}$
	$6.7 \times 10^{-2}$	$2.8 \times 10^{-2}$	2.5	$2.3 \times 10^{-1}$
	$4.3 \times 10^{-2}$	$1.0 \times 10^{-2}$	2.3	$6.3 \times 10^{-2}$

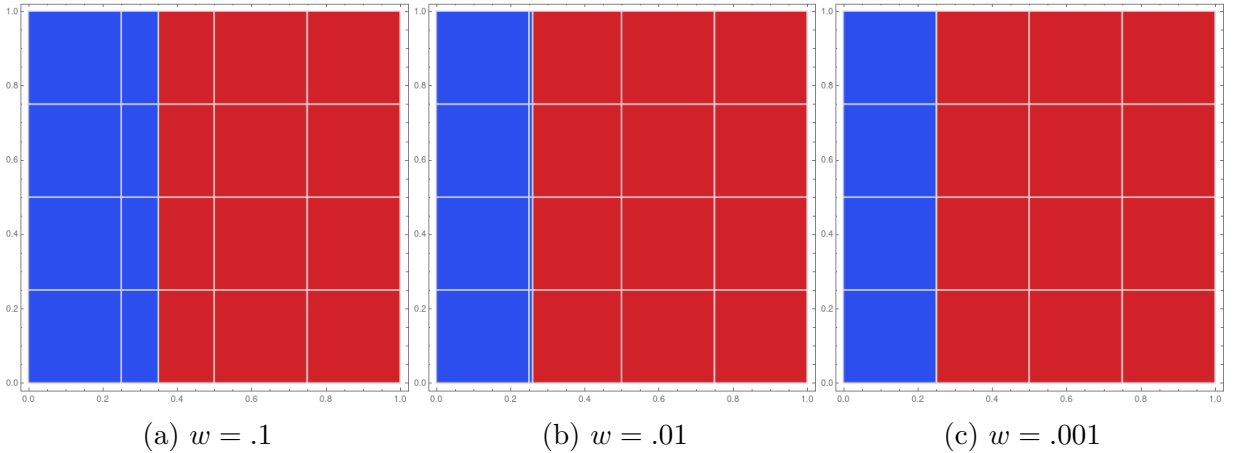
Arithmetic	$h$	$e_{\text{AH}}^{\ell^2}$	$\rho$	$e_{\text{AH}}^\infty$
	$3.0 \times 10^{-1}$	4.9		17
	$2.5 \times 10^{-1}$	5.0		17
	$1.3 \times 10^{-1}$	4.9		17
	$8.3 \times 10^{-2}$	4.7		17
	$6.7 \times 10^{-2}$	4.4		16
	$4.3 \times 10^{-2}$	$9.7 \times 10^{-1}$	3.5	5.7
Harmonic	$h$	$e_{\text{HH}}^{\ell^2}$	$\rho$	$e_{\text{HH}}^\infty$
	$3.0 \times 10^{-1}$	2.3		15
	$2.5 \times 10^{-1}$	1.7	1.6	16
	$1.3 \times 10^{-1}$	$7.3 \times 10^{-1}$	1.2	12
	$8.3 \times 10^{-2}$	$4.8 \times 10^{-1}$	1.0	12
	$6.7 \times 10^{-2}$	$3.4 \times 10^{-1}$	1.6	9.4
	$4.3 \times 10^{-2}$	$1.6 \times 10^{-1}$	1.7	8.2

We see that ASC(0) starts to converge linearly with respect to  $\ell^2$ -norm once  $h < 6.7 \times 10^{-2}$ . ASC(1) demonstrates a robust behavior and shows the convergence rate close to quadratic with respect to  $\ell^2$ -norm as in previous examples, and performs better than homogenization approaches.

#### 4.4 Algebraic robustness

In this section, we study the dependence of the condition number of matrix  $\mathbf{S}_{\mathcal{T}}$  on the position of the material interface against the background mesh. For this purpose, we solve the diffusion problem (1) in the unit square with  $\partial\Omega = \partial\Omega_D$ ,  $\mathbf{K} = k\mathbf{I}$ ,  $k = 1$  on the left part and  $k = 0.1$  on the right. We keep the mesh fixed, and change the position of the interface so that the minimal length  $w$  of mini-faces gets smaller,  $w = 10^{-1}, 10^{-2}, \dots, 10^{-5}$  (see Figure 10).

Figure 10: Distribution of materials leads to different values of the minimal length  $w$  of mini-faces



Numerical results are shown in Table 4. We observe that the condition number  $\kappa_{\text{ASC}(0)}$

Table 4: Condition numbers of ASC(0) / ASC(1) system matrices (15)

$w$	$\kappa_{\text{ASC}(0)}$	$\kappa_{\text{ASC}(1)}$	$\tilde{\kappa}_{\text{ASC}(1)}$
$10^{-1}$	41.0	1 730	41.0
$10^{-2}$	45.2	2 817	45.1
$10^{-3}$	48.3	16 391	48.3
$10^{-4}$	49.0	152 325	49.0
$10^{-5}$	49.1	$1.5 \times 10^6$	49.1

of  $\mathbf{S}_{\mathcal{T}}$  for ASC(0) levels off if  $w$  gets smaller. The condition number  $\kappa_{\text{ASC}(1)}$  of ASC(1) depends on  $w$  and behaves as  $O(w^{-1})$  for  $w \rightarrow 0$ . A closer look at the spectrum of  $\mathbf{S}_{\mathcal{T}}$  reveals that the growth of the condition number for ASC(1) is due to presence of only few (three for this example) small eigenvalues, which tend to zero. To illustrate this, Table 4 shows the “effective” condition number of  $\mathbf{S}_{\mathcal{T}}$  that is defined as

$$\tilde{\kappa}_{\text{ASC}(1)} = \mu_{\max} / \mu_3$$

where  $\mu_{\min} = \mu_0 \leq \mu_1 \leq \dots \leq \mu_{\max}$  are the eigenvalues of  $\mathbf{S}_{\mathcal{T}}$  of ASC(1). From this results we see that the effective condition number of ASC(1) stays bounded with respect to the interface position and is close to the condition number of ASC(0). We hypothesize that the number of outliers in the spectrum of  $\mathbf{S}_{\mathcal{T}}$  is proportional to the number of multi-material cells with small cuts.

It is well-known that the presence of a few outliers in the spectrum does not affect the *asymptotic* convergence of the conjugate gradient (CG) iterative methods, see, e.g., [?]. Indeed, in our experiments the CG method (with algebraic multigrid preconditioner) was found to be equally effective for solving systems of algebraic equations resulting from ASC(0) and ASC(1).

## 4.5 Unsteady problem

We finally apply the ASC methods to simulate the time-dependent diffusion problem. In the mixed form, the problem reads

$$\begin{cases} \mathbf{K}^{-1} \mathbf{u} + \nabla p = 0 & \text{in } \Omega, \\ \nabla \cdot \mathbf{u} + \frac{\partial}{\partial t} p = f & \text{in } \Omega \end{cases} \quad (27)$$

for  $t \in (0, T]$  with initial data  $p(\mathbf{x}, 0) = p_0(\mathbf{x})$  and boundary data as in (2). After discretizing in time by the implicit Euler method, the problem takes the form (1)–(2) with  $c = |\Delta t|^{-1}$  and we apply the spacial discretization described in section 3. For the purpose of comparison, we apply arithmetic and harmonic homogenization methods followed by a MFD discretization.

The computational domain is the same as in section 4.3.2 with the example of three different materials.  $\Omega_1 = \{\mathbf{x} : \|\mathbf{x} - \mathbf{x}_0\| < 0.15\}$ ,  $\Omega_2 = \{\mathbf{x} : 0.15 < \|\mathbf{x} - \mathbf{x}_0\| < 0.2\}$ , and  $\Omega_3 = (0, 1)^2 \setminus (\bar{\Omega}_1 \cup \bar{\Omega}_2)$ . The diffusion tensor is set to be  $\mathbf{K}_i = k_i \mathbf{I}$ ,  $k_1 = 10$ ,  $k_2 = 0.002$ , and  $k_3 = 1$ .

We prescribe Dirichlet boundary data  $g_D = 1$  on the left side of the unit square, while right, top, and bottom sides are prescribed no-flux boundary condition,  $g_N \equiv 0$ . The external source term is zero,  $f \equiv 0$ . The initial concentration is set to be

$$p_0(x, y) = (1 - x)^{10}.$$

The equilibrium state for  $t \rightarrow \infty$  is obviously  $p \equiv 1$ . In our computations, we set the final time  $T = 5$ .

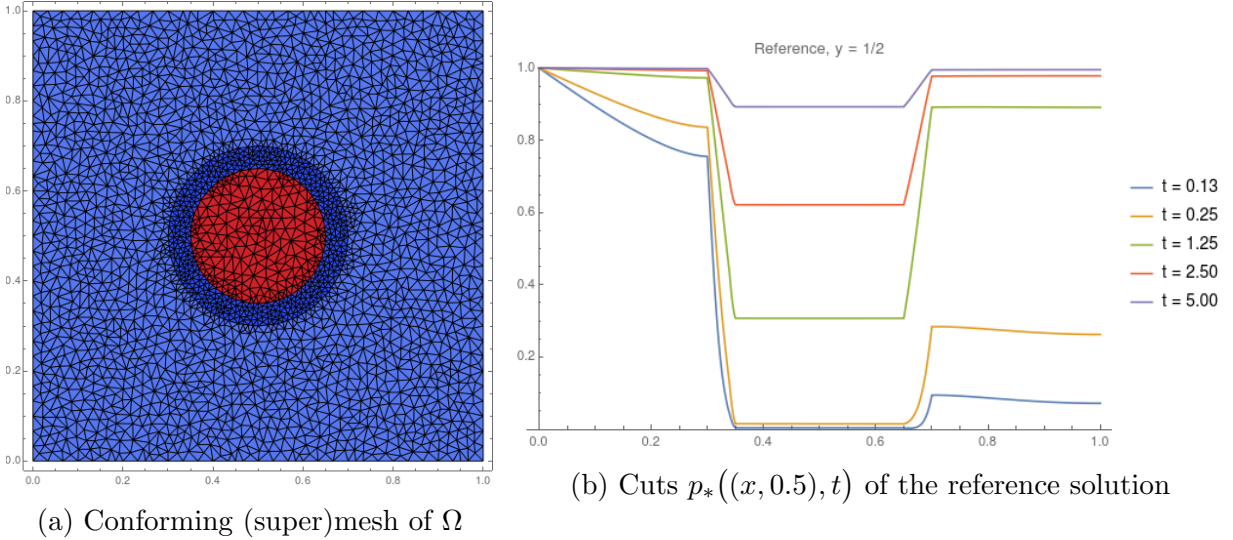


Figure 11: Triangulation of  $\Omega$  used to obtain the reference solution and cuts of the reference solution for  $t \in \{0.13, 0.25, \dots, 5\}$

We first compute solution  $p_*$  to the problem (27) using  $P_2$  finite element method on sufficiently fine mesh consisting of 4908 triangles. This mesh is illustrated in Figure 11 (left). The reference mesh is consistent with material interfaces so it consists only of single-material cells. Time step  $\Delta t$  is chosen as  $T/40$ . This solution was found to be (almost) mesh independent and will serve as the reference solution. The center cutline profiles  $p_*((x, 0.5), t)$  are shown in the Figure 11 (right) for several values of  $t \in (0, T]$ .

For ASC(0), ASC(1), arithmetic and harmonic homogenization methods we use two Voronoi meshes with  $h = 1.5 \times 10^{-1}$  (124 base cells) and  $h = 8.1 \times 10^{-2}$  (465 base cells). The coarse mesh contains 20 multi-material cells and two macro-faces sharing three materials. The fine mesh contains 50 multi-material cells and no three material macro-faces. For all these methods we use 20 time steps,  $\Delta t = T/20$ . Results are shown in Figures 12–14.

From the figures it is easy to appreciate that among all the methods only ASC(1) provides a reasonable approximation for the coarse mesh, cf. Figures 12. Numerical solution computed with ASC(0) overestimates incoming fluxes for the ring. This solution converges to the equilibrium state  $p_h \approx 1$  at approximately  $t = 3.75$ , which is significantly earlier than the time when the same state is achieved by the reference solution. Note that the coarse mesh contains faces with three materials, and we saw already that ASC(0) may fail to converge for this case even for stationary examples.

We tried replacing Voronoi mesh with a triangulation such that the number of triangles is close to the number of the polygonal cells in the fine Voronoi mesh (456 elements for

the triangular mesh v.s. 465 for the Voronoi mesh); the achieved difference is that the triangular mesh has faces with three materials, and Voronoi mesh does not. Nevertheless, ASC(0) performed poorly for this example converging to the steady-state at approximately  $t = 3$ .

Arithmetic homogenization performs poorly for both mesh levels (even finer mesh near the inclusions is required to provide reasonably accurate solution). Harmonic homogenization shows reasonable results only for the fine mesh.

In Figure 14 we present the  $\ell^2$ -norm of the error  $p_* - p_h$  computed for the inclusion  $\Omega_1 \cup \Omega_2$  as a function of time. Since all numerical solutions eventually converge to the same steady state, numerical errors for any method decrease for large enough time. On earlier stages ASC(1) outperforms all methods on the coarse mesh and provides comparable results with ASC(0) scheme and the harmonic homogenization approach on the fine mesh.

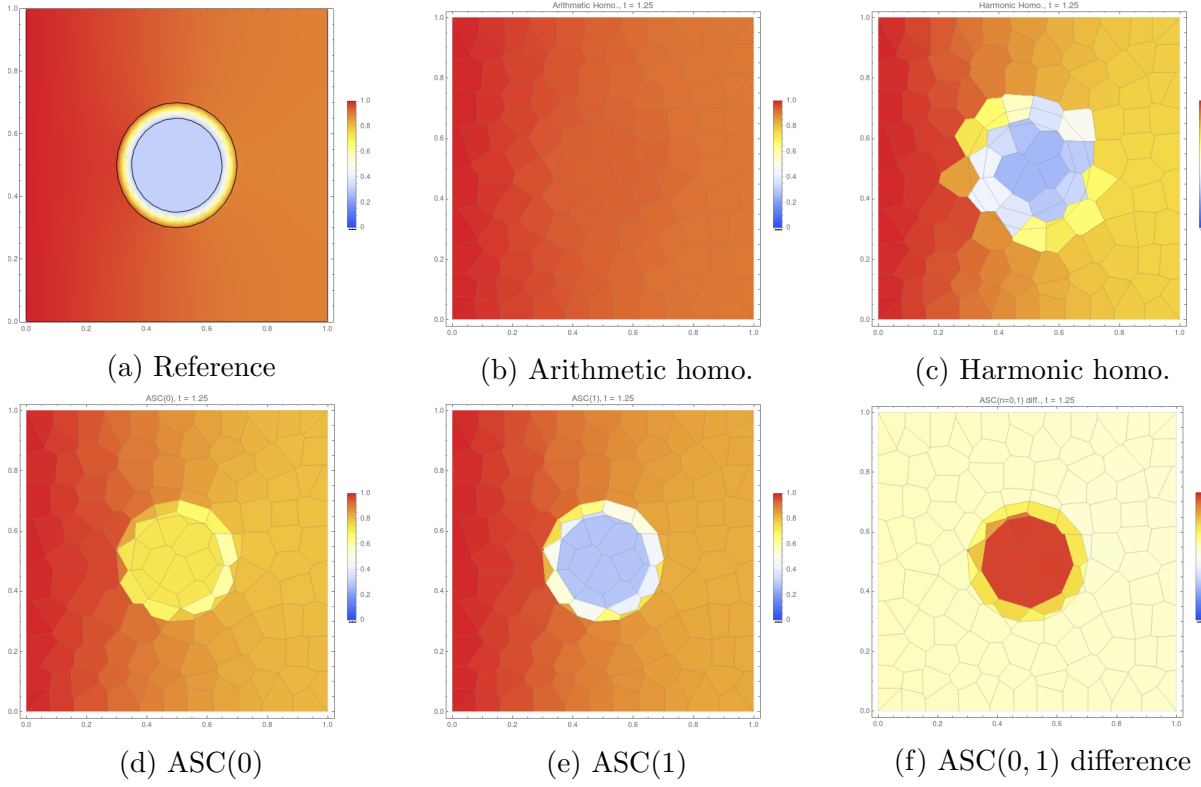


Figure 12: Comparison of the discrete solutions  $p_h$  for  $h = 1.5 \times 10^{-1}$ ,  $t = 1.25$

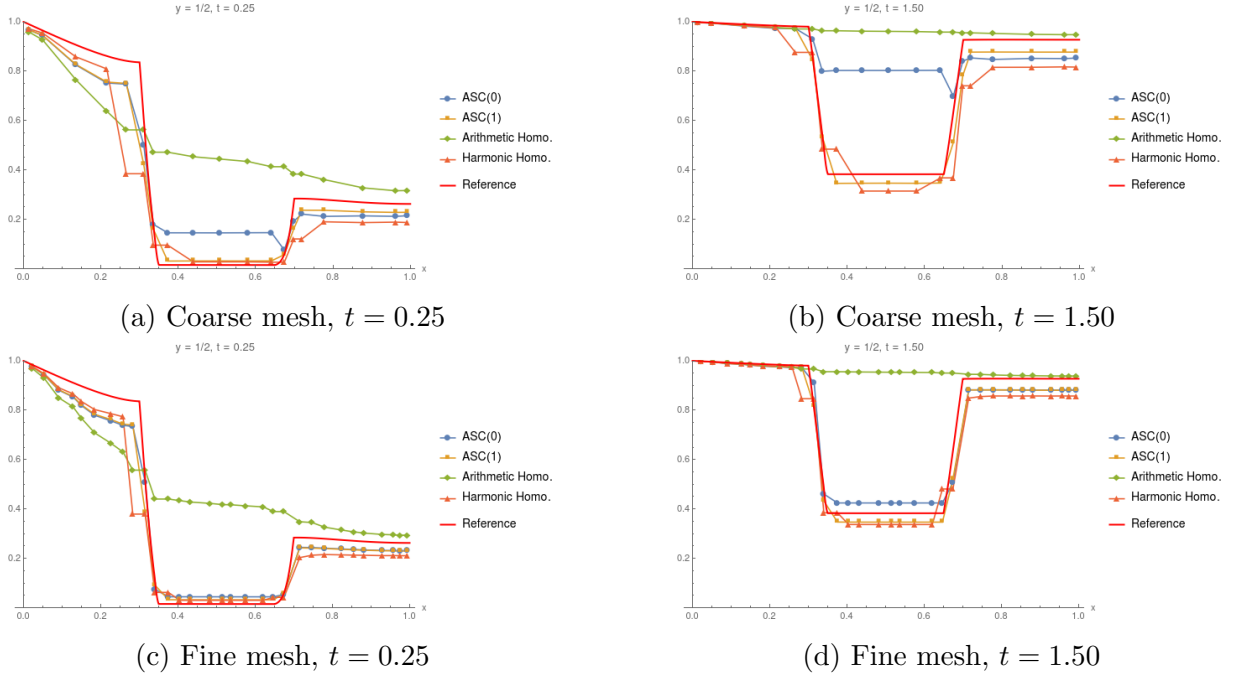
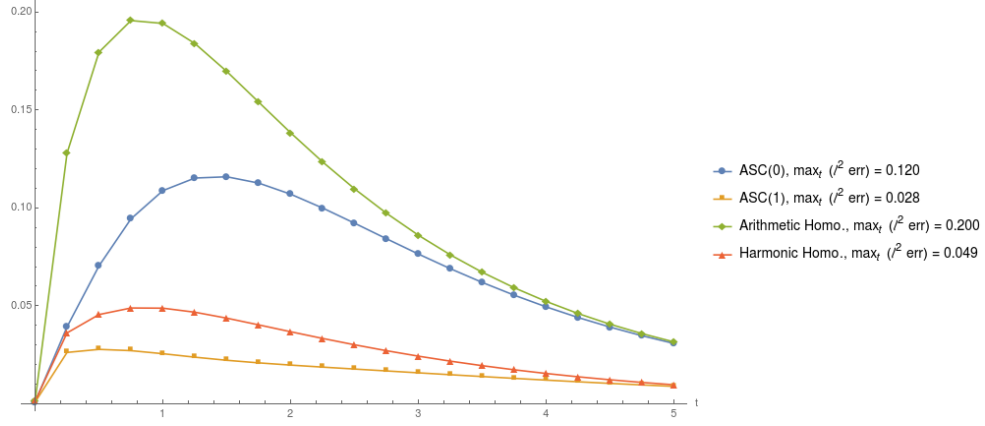
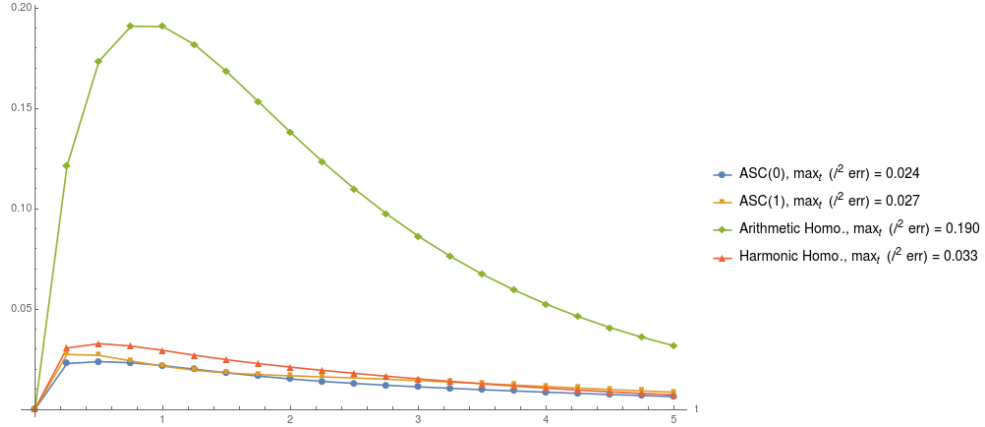


Figure 13: Comparison of the cuts  $p_h((x, 0.5), t)$  of discrete solutions for coarse and fine meshes,  $h = 1.5 \times 10^{-1}$  and  $h = 8.1 \times 10^{-2}$





(a) Coarse mesh



(b) Fine mesh

Figure 14:  $\ell^2$ -norm of the error computed for the inclusion  $\Omega_1 \cup \Omega_2$  for coarse and fine meshes,  $h = 1.5 \times 10^{-1}$  and  $h = 8.1 \times 10^{-2}$

## Acknowledgments

Funded by the Department of Energy at Los Alamos National Laboratory under contracts DE-AC52-06NA25396 and the DOE Office of Science Advanced Computing Research (ASCR) program in Applied Mathematical Sciences. Alexander Zhiliakov acknowledges the internship opportunity in the Los Alamos National Laboratory.